

Cite this: *RSC Adv.*, 2015, 5, 8077

Effect of ceria on the organization and bio-ability of anatase fullerene-like crystals†

 Noel Gravina,^a Juan M. Ruso,^b Doris A. Mbeh,^c L. 'Hocine Yahia,^c Yahye Merhi,^d
Javier Sartuqui^a and Paula V. Messina^{*a}

The nanostructure and the oxygen storage capacity against reactive oxygen species (ROS) are essential features to take into account during the design of a new material that will be used as the basis of novel therapeutic technologies. Here we evaluate the incorporation of nano-ceria, which has a demonstrated ability to scavenge free radicals under physiological conditions comparable to those observed for superoxide dismutase and catalase, to TiO₂ crystalline assemblies. The material was planned to merge the scavenging properties of CeO₂ on a specifically designed structured TiO₂ substrate. The presence of Ce atoms has a clear influence on the materials' morphologies, distorting the anatase crystal lattice and inducing the formation of fullerene-like structures. The cytotoxicity of the materials against L929 fibroblasts after 24 hours of cell culture was evaluated. Both structural and oxidative properties of the materials have a clear effect on fibroblast viability; in fact it was demonstrated that cellular proliferation can be modulated by varying the Ce³⁺/Ti⁴⁺ molar ratio.

Received 21st November 2014
Accepted 19th December 2014

DOI: 10.1039/c4ra15031g

www.rsc.org/advances

1. Introduction

Cerium oxide (Ceria) based nano-materials have attracted the interest of the scientific community all around the globe and have been used efficiently in various advanced technologies such as catalysis and photo-catalysis, solid-oxide fuel cells, smart glass materials, vehicles gas treatments, sensors, high temperature superconducting resources, ultraviolet blocking and sunscreen cosmetics and luminescent or optic tools.^{1,2} The use of CeO₂ for most of these applications depends on its ability to release and uptake oxygen. Ceria has large oxygen storage capacity depending on Ce⁴⁺ and Ce³⁺ redox cycles.^{1,3} Moreover, the reduction of grain size in the nano-regime intensifies the optical and electrical properties compared to

coarse bulk crystals due to the presence of surface defects, phonon confinement and internal strain.¹ Actually, the exceptional ability of ceria nanoparticles to switch oxidation states between III and IV under physiological conditions has emerged as a fascinating and lucrative material in biomedical science.^{4,5} The ability of nano-ceria to switch between oxidation states is comparable to that of biological antioxidants.^{6–8} This capability imparts nano-ceria with a very important biological property: the free radical scavenging. For this reason nano-ceria has been tested in both *in vitro* and *in vivo* models to determine its ability to protect cells against reactive oxygen species (ROS) and oxidative stress.^{4,6,7} The application of ceria nanoparticles in the treatment of spinal cord injury and other central nervous system-based neuron degenerative diseases has proven the biological importance of nano-ceria beyond suspicion.^{5,9} Additionally, current studies have demonstrated that ROS generation is a key modulator of cell function and that oxidative status influences the pathophysiology of mineralized tissues.^{10,11} Additional studies will be needed to explore whether manipulation of the redox balance in bone cells represents a useful approach in the design of further therapies for bone diseases. In ceria, a size dependency of lattice parameters take place due to the dissimilarity in Ce⁴⁺ and Ce³⁺ sizes. That results in the modification of crystalline lattice and in the development of strain arising from loss of oxygen from surface region.¹ This characteristic can be used to manipulate the material structural properties; which are especially valuable in the development of novel orthopedic implantable devices because of the strong effect of material surface morphology on the viability, spread and proliferation of cells.¹²

^aDepartment of Chemistry, Universidad Nacional del Sur, INQUISUR-CONICET, 8000, Bahía Blanca, Argentina. E-mail: pmessina@uns.edu.ar; Fax: +54 291 4595160; Tel: +54 291 4595159

^bSoft Matter and Molecular Biophysics Group, Department of Applied Physics, University of Santiago de Compostela, Santiago de Compostela, 15782, Spain

^cLaboratory for Innovation and Analysis of Bio-Performance, École Polytechnique de Montréal, C.P. 5079, Succursale Centre-Ville, Montréal, Quebec, Canada H3C 3A7

^dMontreal Heart Institute & Université de Montréal, 5000 rue Belanger, Montréal, Quebec, Canada H1T 1C8

† Electronic supplementary information (ESI) available: Material structural characterization: EDX; nano-particles size distribution histograms; $d_{\text{Ti-O}}^{\text{eq}}$, $d_{\text{Ti-O}}^{\text{pp}}$, $d_{\text{O-O}}^{\text{eq}}$, $d_{\text{O-O}}^{\text{sh}}$, $d_{\text{O-O}}^{\text{ush}}$ distances computed considering the extreme planar condition with $u = 0.25$; detailed information used in molecular modeling and Rietveld method; FT-Raman spectra; photoluminescence spectra. Fibroblast and adenocarcinomic human alveolar basal epithelial cells (A549) proliferation in the presence of Ce-doped TiO₂ fullerene-like materials. See DOI: 10.1039/c4ra15031g

Based on the information of that Ti and Ti alloys are widely used for many orthopedically applications¹³ and that the use of TiO₂ coatings would increase their metallic surfaces bioactivity,¹⁴ the authors prepared and characterized different types of CeO₂-TiO₂ materials.¹⁵ It was detected that the employment of a bulkier organic ceria precursor during the synthesis stage has several effects on: the morphology, the topology, the polymorphism and the oxygen storage capacity of titanium dioxide nano-crystals assemblies. Such effects indirectly favor the rapid formation of a hydroxyapatite layer composed of sphere-like globules of 3–5 μm in diameter essential for bone-bonding on the material surface.¹⁵ Herein, we go further evaluating the influence of CeO₂ presence in the distortion of titanium dioxide crystalline planes to provide a superior biological compatibility to the implantable materials; and the effect of material oxygen storage capacity in the viability and proliferation of cells. We have conducted a methodological phase behaviour analysis on several systems conditions, showing that under specific circumstances the ceria presence induces on anatase crystal a hollow, stable and closed structure characteristic of inorganic fullerene-like (IF) assemblies usually produced from compounds with (2D) layered arrangement like the metal dichalcogenides.^{16–22} Unlike the metal dichalcogenides compounds, TiO₂ is not a layered material and TiO₂ “inorganic fullerene-like structures”²³ can be obtained only under elaborated synthetic procedures.^{24–31} The obtained final products were characterized by field emission scanning electron microscopy (FE-SEM), X-ray diffraction (XRD), high resolution transmission electron microscopy (H-TEM), Fourier transform infrared (FT-IR), resonance Raman and fluorescence (F) spectroscopy. Cell viability and morphology studies on fibroblast, selected on basis of their participation in wound healing, were conducted to certify the material bio-compatibility and its future use in biomedical strategies. The study presented here offers some novel information inside the complex formation process of inorganic fullerene-like nanostructures. It was concluded that, despite the bibliographical evidences, IF-TiO₂ structures crystallized in anatase polymorph since the early steps of the synthesis and it is not a consequence of the calcination process but the effect of the presence of cerium atoms. Moreover cerium atoms' presence is the driving force off the crystal planes folding, leading to the formation of large fullerene-type structures. Also, it was demonstrated that the material structure along with its oxygen storage capacity has a clear effect on fibroblast survival and proliferation. Literature data demonstrated a large spectrum of medical applications that could benefit from the superior tribological behavior of IF structures.³² A variety of medical devices has been coated and tested so far, developing new clinical purposes, including coatings for orthodontic wires,^{17,33} catheters, heart valves, and stents.^{34,35} The information given provides a step forward to the construction of engineered scaffolds designed to exhibit novel oxygen storage capacity and structural properties to control cellular proliferation.

2. Materials and methods

2.1. Reagents

Hexadecyl-trimethyl ammonium bromide (CTAB, MW = 364.48 g mol^{−1}, 99% Sigma), *n*-heptane (MW = 100.21 g mol^{−1}, δ = 0.684 g cm^{−3}, Merck), butyl alcohol (BuOH, MW = 74.12 g mol^{−1}, δ = 0.810 g cm^{−3}, Merck), cerium valerate (Ce(Val)₃, MW = 443.1 g mol^{−1}) and titanium(IV) isopropoxide (TTIP, Ti(IV)(OiPr)₄, MW = 284.22 g mol^{−1}, δ = 0.960 g cm^{−3}, 97% Aldrich) were used without further purification. Commercial TiO₂ anatase (99%) was purchased from Sigma Aldrich. For cell culture and treatments, high-sugar Dulbecco's modified Eagle's medium (DMEM), fetal bovine serum (FBS) and Penicillin-streptomycin were purchased from American Type Culture Collection (ATCC). Trypsin-EDTA solution (1×) was purchase from Gibco and PrestoBlue® was purchase from Invitrogen. CdTe-Quantum Dots (CdTe-DQs) were purchased from Vive Nano Inc. (formerly Northern Nanotechnologies Inc.). For microemulsion preparation, only triple-distilled water was used.

2.2. Material synthesis

Selected synthesis conditions were carefully investigated in previous works.^{36–38} Experiments were performed on water/CTAB-BuOH/*n*-heptane microemulsion systems using a single microemulsion method.³⁹ As the critical micelle concentration (CMC) of CTAB⁴⁰ in both oil and water is low compared to the concentration used here, it can be assumed that all the surfactant molecules are localized at the interface between water and oil. According to the phase diagram of the pseudo-ternary system (water/CTAB-BuOH/oil),⁴¹ we worked inside the isotropic fluid phase (L2) where the structure of aggregates are only spheres. The composition of the final microemulsion systems are given here in terms of *W*₀ = water/surfactant; *S*₀ = oil/surfactant; BuOH/surfactant; TTIP/surfactant and Ce(Val)₃/TTIP ratios.

During the synthetic procedure a microemulsion “A” (containing CTAB, BuOH, oil and aqueous phases) was mixed with a solution “B” formed by the dissolution of TTIP in the oil phase (*n*-heptane) without stirring and left to equilibrate for 20 minutes to follow the reaction:



For the synthesis of different Ce-doped TiO₂ materials (K1, K2, K3, K4, K5, K6 and K7) varied amounts of Ce (Val)₃ were added respectively to microemulsion “A” before mixing with solution “B”. A summary of the reagent quantities utilized during the synthesis procedure were shown in Table 1. The incorporation of different proportions of Ce(Val)₃ to the microemulsion system were tested, verifying that more than 3 wt% of Ce(Val)₃ knock down the microemulsion system. The resulting gels were left for 24 h in an autoclave at 100–120 °C. The obtained materials were filtered, washed with triple-distilled water and left to dry at room temperature. Finally, they were calcined for 7 h at 650 °C in an air flux.

Table 1 Synthetic conditions of Ce-anatase fullerene-like materials

Sample	Microemulsion "A"					Solution "B"		Final microemulsion conditions				
	wt% CTAB	wt% ButOH	wt% water	wt% oil	wt% Ce(Val) ₃	wt% oil	wt% TTIP	S ₀	W ₀	TTIP/CTAB	ButOH/CTAB	Ce(Val) ₃ /TTIP
K1	9.68	47.06	9.68	33.68		63.4	36.6	25.3	20.1	2.5	24	
K2	9.68	47.05	9.68	33.57	0.02	63.4	36.6	25.3	20.1	2.5	24	6.0×10^{-4}
K3	9.68	47.05	9.68	33.57	0.02	78.3	21.7	25.3	20.1	1.2	24	1.2×10^{-3}
K4	9.67	47.02	9.67	33.55	0.09	78.3	21.7	25.3	20.1	1.2	24	6.0×10^{-3}
K5	9.66	46.98	9.66	33.53	0.17	78.3	21.7	25.3	20.1	1.2	24	0.012
K6	9.60	46.65	9.60	33.29	0.86	78.3	21.7	25.3	20.1	1.2	24	0.06
K7	9.52	46.25	9.52	33.00	1.71	78.3	21.7	25.3	20.1	1.2	24	0.12
K8	9.48	46.05	9.48	32.86	2.13	87.8	12.2	25.3	20.1	0.6	24	0.30

2.3. Material characterization

2.3.1. Field emission scanning electron microscopy (FE-SEM). Surface morphology was evaluated using a field emission scanning electron microscope (ZEISS FE-SEM ULTRA PLUS). To acquire all the SEM images a Secondary Electron Detector (In lens) was used. The accelerating voltage (EHT) applied was 3.00 kV with a resolution (WD) of 2.1 nm. Local compensation of charge (by injecting nitrogen gas) was applied avoiding the sample staining. Quantitative information about surface elemental composition was determined by the associated X-ray energy-dispersive (EDX) spectrometer. Powdered samples were placed on aluminum supports.

2.3.2. High resolution transmission electron microscopy (HTEM). High resolution transmission (H-TEM) microphotographs were taken using a ZEISS Libra 200 FE OMEGA transmission electron microscope operated at 200 kV with magnification of 1 000 000 \times . Observations were made in a bright field. Powdered samples were placed on carbon supports of 2000 mesh. The equipment is provided with a electron diffraction (ED) system, d -spacing is computed based on the Bragg Law derived equation ($rd = L\lambda$), where " r " is the spot distance in the ED pattern, and $L\lambda = 1$ is the camera constant.

2.3.3. X-ray powder diffraction. Powder X-ray diffraction (XRD) data were collected with a Philips PW 1710 diffractometer with Cu K α radiation ($\lambda = 1.5418$ nm) and Graphite monochromator operated at 45 kV; 30 mA and 25 °C. The rutile to anatase ratio (F_r) was computed from the XRD intensity data by the following equation:⁴²

$$F_r = 1 - \left(1 + 1.265 \frac{I_{\text{rutile}(110)}}{I_{\text{anatase}(101)}} \right)$$

Anatase crystals corresponds to the tetragonal crystal family ($a = b \neq c$; $\alpha = \beta = \gamma = 90^\circ$). The lattice geometry parameters (a , c) and the volume of the direct unit cell (V), were computed using the symmetric (101) and (200) reflections:

$$\frac{1}{(d_{hkl})^2} = [(h^2 + k^2)/a^2] + [l^2/c^2],$$

$$V = a^2c$$

where, d_{hkl} is the interplanar spacing computed by the Bragg equation ($\lambda = 2d_{hkl} \sin \theta$) and (hkl) are the Miller index of the symmetric reflections used in the calculus.⁴³

2.3.4. FT-IR Raman. The room temperature Raman scattering measurements were carried out on a RENISHAW Raman, "In via Reflex" model, spectrometer with an Argon ion laser ($\lambda = 514$ nm) as the excitation light. The slits were adjusted so that the resolution was 1 cm⁻¹. The scattered light was collected in the backscattering geometry using a liquid nitrogen cooled (CCD) detector. Prior to each measurement, the spectrometer was calibrated using a mercury lamp.

2.3.5. Fluorescence spectroscopy. Fluorescence spectra were recorded at 25 °C by a Varian Cary Eclipse spectrofluorometer under excitation by UV light at 220 nm, using a 1 cm path length quartz cell. The spectrum was obtained after the materials sonication in ethanol to yield homogeneous dispersions. Pure ethanol solution was used as black.

2.4. Nanoparticles (NPs) preparation for cytotoxicity tests

Commercial TiO₂ anatase and Ce-TiO₂ powders were sterilized in autoclave for 30 min at 121 °C, freshly diluted in PBS and sonicated for 2 hours in order to obtain a homogeneous stock dispersion with a final concentration of 1 mg mL⁻¹. Immediately before using in cell treatments, the previously resuspended NPs were diluted in DMEM supplemented with 5% of FBS to obtain a working final concentration of 100 μ g mL⁻¹. CdTe-DQs were diluted in a 500 μ g mL⁻¹ final concentration using DMEM supplemented with 5% of FBS as a solvent.

2.5. Cell culture

Mouse Fibroblast cells (L929) and Adenocarcinomic Human Alveolar Basal Epithelial cells (A549) were obtained from the American Type Culture Collection (ATCC). Both cell lines were cultured in a 25 cm³ polyethylene flask using DMEM supplemented with 10% of Fetal Bovine Serum (FBS), 1% Penicillin/Streptomycin, and maintained at 37 °C in a 5.0% CO₂ humidified environment. The culture medium was routinely replaced every 2 days and the cells were split by adding 2 mL trypsin-EDTA when reaching confluence of 70–80%.

2.6. Cytotoxicity

Cell viability in presence of different materials was determined in 96-well plates using PrestoBlue® Cell Viability Reagent according to manufacturer's protocol. Briefly, 100 μL of freshly trypsinized cells were seeded in a 96-well plate in a density of 5000 cells/well and incubated at 37 °C and 5.0% CO_2 . After 24 hours, cell culture media was completely removed, replaced with freshly prepared nanoparticles suspension and continued culturing for 24 hours. For cell viability testing, 10 μL of dye were added to each well and the plates were placed for 30 min in a 37 °C incubator; then, the reaction mixtures were transferred to an opaque 96-well plate and the fluorescence intensity was immediately measured by Biotek Synergy 2® microplate reader at excitation and emission wavelengths of 560 nm and 590 nm, respectively. A "no cell" control was used as a baseline for fluorescence values, CdTe-QDs treated cells were used as a Positive Control in an effective 500 $\mu\text{L mL}^{-1}$ concentration (data experimentally determined in our laboratory) and untreated cells were used as a Negative Control for normalization. The cells were observed and microscopic photographs were taken using an Olympus CKX41 inverted microscope coupled to a Q-Imaging QICAM digital camera. Results were expressed as the mean \pm standard deviation for 4 replicates as a percentage of negative control (taken as 100%).

3. Results and discussion

3.1. Ce-anatase fullerene-like nanostructures

The key to developing and exploiting new nanostructured materials lies in an increased understanding of how synthesis conditions affect their properties in order to tailor them to specific needs; accordingly the knowledge of nanostructure formation mechanism is of particular importance. The proposed bottom-up method used here to generate the inorganic fullerene Ce-anatase structures consists in three basic steps to control their growth and their stacking morphology: (i) microemulsion preparation, (ii) hydrothermal treatment and (iii) annealing. The adequate combination of the selected parameters determined for each of the above mentioned steps exerts a delicate control over the micro-droplets interfacial elasticity, the exchange of reactive species and consequently on the final material characteristics. Descriptions of selected synthesis condition steps and their effect on the final material structures are shown in the ESI.† Fig. 1a and b show a representative SEM image of the obtained IF structures after annealing at 650 °C during 6 h in an air flux. The single-crystalline nanoparticles are normally aggregated, although individual structures can be separated with extended sonication. Energy-dispersive X-ray (EDX) measurements, Fig. 1c, indicate that the basic components of all the samples were Ti, Ce and O. A more detailed EDX analysis is shown in ESI.† The typical high-resolution TEM (H-TEM) images of IF structures are shown in Fig. 2. The layered structure and the hollow-morphology of these IF structures are quite clear from the obtained photographs, while their size and shape are variable to some extent. The Ce/Ti molar ratio seems to be responsible of

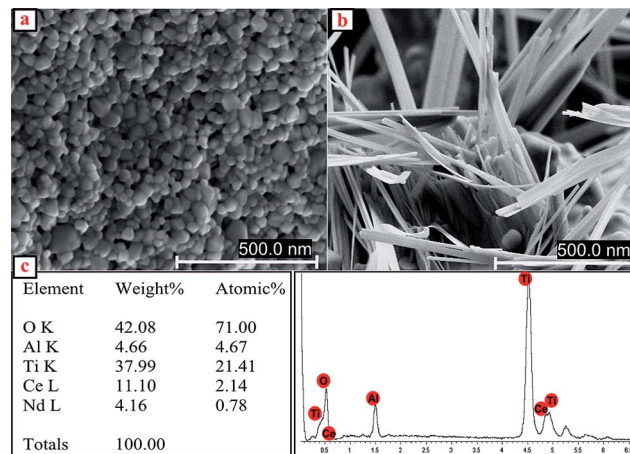


Fig. 1 Scanning electron microscopy (SEM) microphotographs of (a) K2 and (b) K8 materials after annealing at 650 °C during 6 h in an air flux. (c) Energy-dispersive X-ray (EDX) of K8 sample.

these parameters' control. As it is shown in Fig. 2a–d, the number of multi-walls forming the quasi-spherical onion-like structures varies from six to fifty as the Ce/Ti molar ratio in the material augment until 6.0×10^{-3} . At the same time the nanoparticles size is increased, *i.e.*, in the samples K1 and K2 the length and width of nanoparticles are about 17 nm and 11 nm respectively; while in K4, the nanoparticles are 58 nm in length and 37 nm in width. Size distribution histograms are shown in ESI.† Also the particles show a reduction of the internal hollow space width, in agreement with the increase of the multi-walls number. As the content of Ce/Ti exceeded the 6.0×10^{-3} value, there was a reduction of multi-walls number to 20, as a maximum, even though the structures became elongated.

It can be seen from Fig. 2e–h that IF structures length expands up to 600 nm as the Ce/Ti molar ratio augment from 0.012 to 0.3. It seems that it is not possible an enlargement of the IF structure with a simultaneously retention of the concentric crystalline layers number. Therefore, the structures get bigger at the expenses of multi-walls number. Accordingly to the mechanism proposed by Tenne *et al.*,²⁰ the existence of Ce atom contaminants possibly reduces or eliminates the strain of bending of TiO_2 layers through the formation of cerium oxide structures at the corners. This effect combined with the restricted crystal growth evolution within the microemulsion droplets lead to the growth of fullerene-like structures dropped from nanoparticles to multi-wall elongated structures, for details see ESI.† In all Ce-doped IF materials, the interlayer distance is about 0.34 ± 0.05 nm resembling to the d-spacing of TiO_2 anatase (101) planes, Fig. 3a and b.

Electron diffraction (ED) analysis taken from Ce- TiO_2 fullerene-like materials confirmed their single-crystalline nature and the interlayer distance, Fig. 3c. A better understanding IF structure and composition can be achieved through the inspection of X-ray diffraction (XRD) patterns; results are shown in Fig. 4. It can be observed that pure TiO_2 material (K1) is formed after annealing by a mixture of anatase and rutile

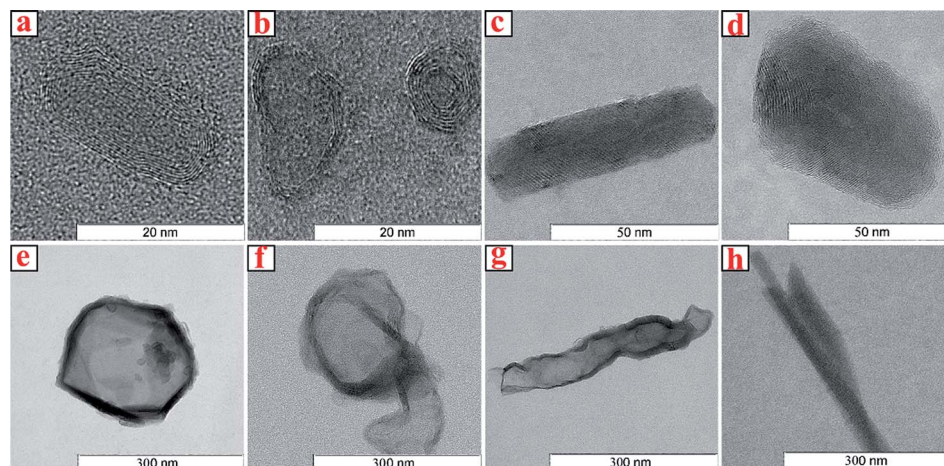


Fig. 2 H-TEM images of different synthesized $\text{CeO}_2\text{-TiO}_2$ samples: (a) K1, (b) K2, (c) K3, (d) K4, (e) K5, (f) K6, (g) K7 and (h) K8.

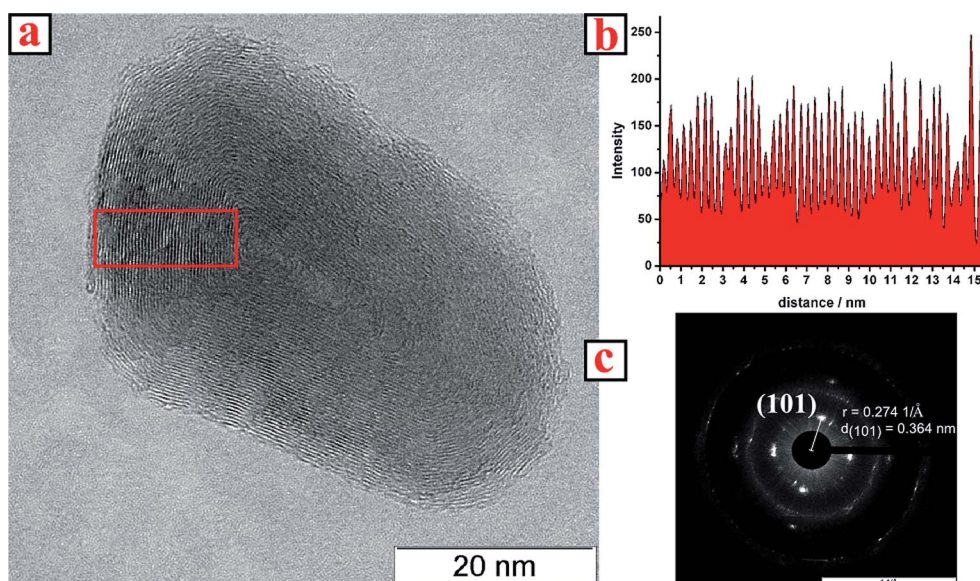


Fig. 3 (a) H-TEM of 6.0×10^{-3} $\text{Ce(Val)}_3/\text{TTIP}$ molar ratio fullerene-like particles (sample K4). (b) Interlayer distance profile and (c) electron diffraction (ED) analysis of the selected area.

($F_r = 0.50$), while all diffraction peaks of Ce-doped IF structures (K2–K8) can be indexed only to anatase phase (JCPDS cards 21-1272). The increase in the full width at half-maximum (FWHM) of peaks and the reduction of their intensities with increasing $\text{Ce}^{3+}/\text{Ti}^{4+}$ molar ratio indicates a decrease in the crystal organization. At any time, no traces of diffraction peaks due to cerium oxide were detected. This is attributed to the length area of distribution of the dopant and the incorporation of Ce atoms into the anatase lattice confirmed for the variation of crystallographic lattice parameters, Table 2. Formally, the anatase structure is one of the prototypes of 6 : 3 lattices, and fit into the tetragonal $I4_1/amd$ space group, Fig. 5a. The conventional unit cell contains four TiO_2 units ($Z = 4$), and there is only one internal parameter related to the oxygen location (fractional coordinate, u).⁴⁴ Titanium atoms occupy the 4a Wyckoff position

at (0, 0, 0), and all oxygen are equivalent and located at the 8c (0, 0, u) position.⁴⁴ The structure is usually described as composed of chains of vertex-linked distorted TiO_6 octahedra that share alternating edges. There are five different Ti–O and O–O distances in these octahedra that can be used in addition to the lattice parameters to characterize the TiO_2 anatase unit cell: (i) a long one involving the two oxygen atoms directed along the c crystallographic axis (apical oxygens), $d_{\text{Ti-O}}^{\text{ap}}$; (ii) a short one, $d_{\text{O-O}}^{\text{eq}}$, with the four equatorial oxygens left, which are arranged forming a tetrahedron squeezed along one of its C_2 axes; (iii) $d_{\text{O-O}}^{\text{eq}}$, between equatorial oxygens; (iv) $d_{\text{O-O}}^{\text{sh}}$, between an apical oxygen and an equatorial oxygen belonging to a shared edge; and (v) $d_{\text{O-O}}^{\text{unsh}}$, between an apical oxygen and an equatorial oxygen of an unshared edge of the octahedron.

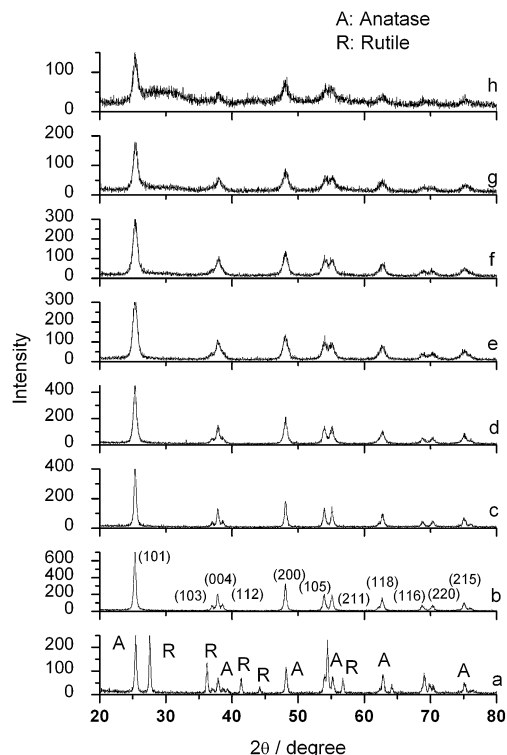


Fig. 4 X-ray diffraction pattern of different synthesized CeO_2 - TiO_2 samples: (a) K1, (b) K2, (c) K3, (d) K4, (e) K5, (f) K6, (g) K7 and (h) K8.

Table 2 Crystallographic parameters of Ce-anatase fullerene-like materials

Sample	$\text{Ce(Val)}_3/\text{TTIP}$	Lattice parameters			
		$a/\text{\AA}$	$c/\text{\AA}$	$V/\text{\AA}^3$	$2\phi/\text{degrees}$
Regular anatase		3.785	9.514	136.308	156.16
K1		3.775	9.540	135.960	156.03
K2	6.0×10^{-4}	3.781	9.530	136.264	156.09
K3	1.2×10^{-3}	3.783	9.503	136.028	156.17
K4	6.0×10^{-3}	3.782	9.449	135.168	156.29
K5	0.012	3.783	9.403	134.594	156.42
K6	0.06	3.783	9.335	133.636	156.58
K7	0.12	3.782	9.214	131.820	156.87
K8	0.30	3.785	9.215	132.032	156.89

Oxygens are located along the C_2 axis of isosceles triangles of Ti atoms, and their distances to them are $d_{\text{Ti-O}}^{\text{eq}}$ (two distances) and $d_{\text{Ti-O}}^{\text{ap}}$ (one distance); the Ti-O-Ti angle between the two shortest bonds is called 2ϕ (traditionally this angle is denoted as θ , we changed it to ϕ to avoid confusion with diffraction angle 2θ), Fig. 5b.

The degree of squeezing is measured by the u parameter; the experimental value of a perfect anatase crystal is 0.208 (ref. 45) while a limiting planar situation corresponding to $u = 1/4$.⁴⁴ The effect of Ce atom incorporation was analyzed on basis of the alteration of Ti-O and O-O distances in the regular anatase octahedra. The algebraic expressions of Ti-O and O-O distances as functions of the lattice parameters a , c , and u are as follows:⁴⁴

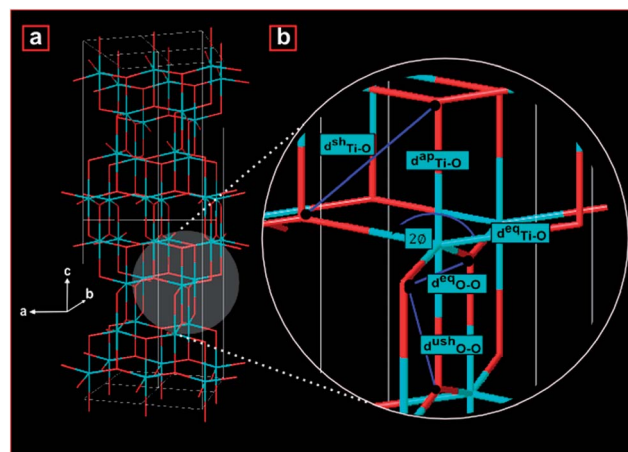


Fig. 5 Schematic representation of (a) anatase crystalline unit cell and (b) Ti-O and O-O distances in a regular tetrahedral anatase crystal.

$$d_{\text{Ti-O}}^{\text{ap}} = cu,$$

$$d_{\text{Ti-O}}^{\text{eq}} = \sqrt{1/4a^2 + c^2(u - 1/4)^2},$$

$$d_{\text{O-O}}^{\text{eq}} = \sqrt{1/2a^2 + c^2(2u - 1/2)^2},$$

$$d_{\text{O-O}}^{\text{sh}} = \sqrt{1/4a^2 + c^2(2u - 1/4)^2},$$

$$d_{\text{O-O}}^{\text{ush}} = \sqrt{1/4a^2 + 1/16c^2},$$

$$2\phi = 2 \arcsin(a/2d_{\text{Ti-O}}^{\text{eq}}).$$

Ti-O and O-O distances were computed considering $u = 0.208$ (regular anatase crystal) and the extreme planar condition with $u = 0.25$. The representation of both set of values *versus* the Ce/Ti molar ratio has the same tendency (ESI†). Regarding the DRX spectra, Fig. 4, and the calculated “ a ” and “ c ” lattice parameters, Table 2, analogous to those obtained for usual anatase crystals we assumed that u should be also similar. So, it can be concluded that the values computed using $u = 0.208$ reproduces the real system better, Fig. 7. The obtained results indicated that all prepared material present a distortion of anatase unit cell. For TiO_2 synthesized material (K1) it can be seen that as a consequence of the folding in IF structures, there was a decrease of a and an increment of c lattice parameters; the inspection of Fig. 7 indicated that this is a result of Ti-O and O-O equatorial distances reduction and a small increment of Ti-O apical length. This distortion persists with small incorporations of Ce atom. At Ce/Ti molar ratio $\geq 6 \times 10^{-3}$ there was a drastic reduction of both apical and equatorial Ti-O and O-O

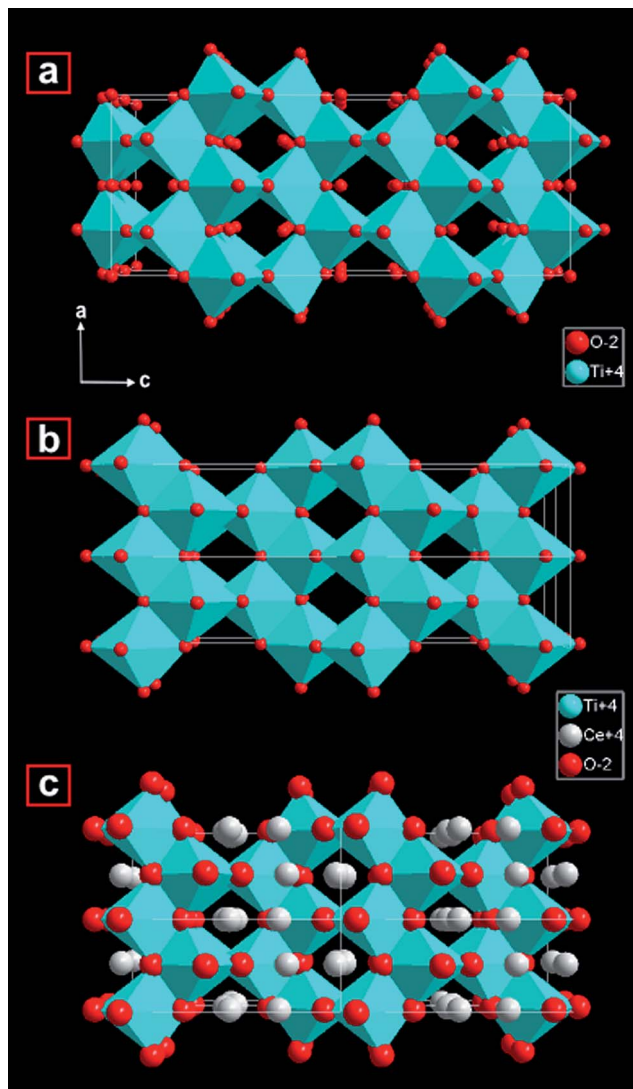


Fig. 6 Schematic representation of (a) regular anatase crystal, (b) K2 sample without considering the incorporation of Ce atom to the anatase structure and (c) K2 sample incorporating the Ce atom to the anatase structure.

distances; shared and unshared O–O lengths are also condensed. The accommodation of bulkier Ce atoms in anatase tetrahedral lattice caused an increment, approximately one degree, of the Ti–O–Ti angle. The overall effects result in the compaction of the unit cell along the *c* crystallographic axis, Table 2.

Using crystal structure refinement from molecular modeling and Rietveld method, detailed information is given in ESI† we have obtained a reproduction of the anatase crystal where the cerium atoms are intercalated along the *c* crystallographic axis among occupied TiO₆ octahedra, Fig. 6c, in completely agreement with experimental data. Among the lanthanide elements, cerium is the only one that forms stable compounds in a tetravalent oxidation state (*i.e.*, Ce⁴⁺). Furthermore the coordination number of the surface Ce⁴⁺ can vary between four and eight, while six and eight is the coordination number of the

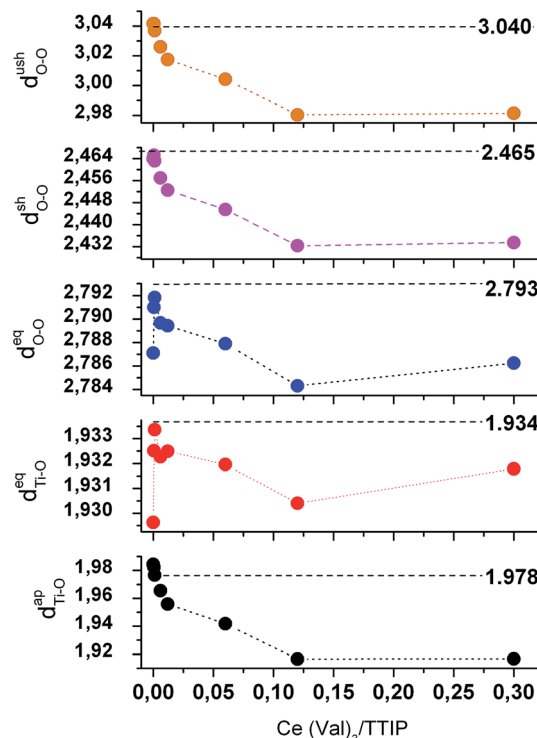


Fig. 7 d_{Ti-O}^{eq} , d_{Ti-O}^{ap} , d_{O-O}^{eq} , d_{O-O}^{sh} , d_{O-O}^{ush} distances variation versus Ce(Val)₃/TTIP molar ratio. Computed considering $u = 0.208$ (regular anatase crystal).

bulk Ce⁴⁺.⁴⁶ Compared with pure anatase, the Ce–O bond lengths for the Ce-doped structure are much larger than those of the Ti–O bonds, which is mainly due to the fact that the atomic radius of Ce is larger than that of Ti (87 pm *versus* 60.5 pm for the effective ionic radii and 101 pm *versus* 74.5 pm for the crystal ionic radii of Ce⁴⁺ and Ti⁴⁺ respectively⁴⁷). This fact would indicate that the Ce doping can induce relative larger local structure modifications.⁴⁸ The change of each Ti–O bond's length from the optimal value implies an expression of energetic facts further than pure geometrical arguments.⁴⁵ Literature result showed that Ce incorporation leads to a decrease of Ti 3d states and enhancement of 4f states in the bottom of conduction band.⁴⁸ The interaction of excess electrons supplied by the 3d orbitals of TiO₂ anatase⁴⁹ with the empty f orbitals of CeO₂ (ref. 50) probably generates the required extra stabilization to the structure which allows compaction of the crystal lattice and the folding in a fullerene-like structure. Raman and fluorescence spectroscopy was employed to have a better insight of the samples' structure. Anatase has six Raman active modes: A_{1g} + 2B_{1g} + 3E_g. Among them, three E_g modes are centered around 141, 197 and 640 cm^{−1} (E_g(1), E_g(2) and E_g(3)); two B_{1g} modes at 400 and 515 cm^{−1} (B_{1g}(1) and B_{1g}(2)). The strongest E_g(1) mode that correspond to the symmetric lattice angular vibrations is the characteristic peak of TiO₂ anatase. Furthermore, rutile has four Raman active modes: A_{1g} + B_{1g} + B_{2g} + E_g. B_{1g} is detected at around 143 cm^{−1}; E_g, 447 cm^{−1}; A_{1g}, 612 cm^{−1} and B_{2g}, 826 cm^{−1}. Regarding their stronger intensity, E_g and A_g are considered the distinctive peaks of TiO₂ rutile.⁵¹ FT-Raman

spectra of undoped TiO_2 (K1 sample), ESI,[†] showed three intense bands centered at $\nu = 141, 466$ and 614 cm^{-1} that can be attributed to the characteristic peaks of anatase and rutile crystalline phases. Meanwhile, only the anatase phase emerges in the Raman spectra of Ce-doped TiO_2 materials (K2–K8), ESI.[†] Similar results were previously obtained from DRX patterns, Fig. 4. Fig. 8a shows the variation of vibration peak $E_g(1)$ intensity with the content of Ce in the material. It can be appreciated a clear reduction of Raman vibrational peak intensity due to the dopant presence, As it was analyzed before, Ce doping causes a crystallite grain modification, leading to an increase in the internal stress. Because of that, the lattice vibration is suppressed and the lattice scattering becomes weak. In addition, there is a Raman blueshift displacement (to higher frequencies) and an asymmetric peak broadening denoted by an increase of full width at half maximum (FWHM) augment with Ce doping. The presence of the dopant in the anatase

matrix causes the unit cell contraction; a similar effect is provoked by the reduction of the crystallite grain size and is called the effect of “phonon confinement”.⁵¹

From DRX and Ti–O and O–O crystalline distances evaluation, it was determined that dopant presence caused the reduction of anatase unit cell along crystallographic c axis, due to the accommodation of Ce atom between occupied TiO_6 octahedra. This location would markedly affect the Raman vibrational bands $B_{1g}(1)$, $B_{1g}(2)$ and A_{1g} that corresponds to Ti and O vibration along c axis direction.⁵² In fact, this alteration can be appreciated from Fig. 8b which shows the effect of dopant concentration on $B_{1g}(1)$, $B_{1g}(2)$ and A_{1g} Raman active modes. At low Ce content, the intensity of $B_{1g}(1)$, $B_{1g}(2)$ and A_{1g} peaks are drastically reduced in contrast to $E_g(3)$; indeed their intensity ratio is inverted compared with pure anatase crystal. Increased amounts of Ce in TiO_2 matrix causes the separation of $B_{1g}(2)$ and A_{1g} bands, generally inseparable because of their peak positions. Similar results were obtained in literature^{53,54} confirming the stabilizing effect of Ce on anatase phase.

Many studies have reported the photo-generation of reactive oxygen species (ROS) on the surfaces of TiO_2 nanoparticles (NPs) in aqueous solutions.⁵⁵ The generation of ROS *in vivo* can virtually damage all types of organic biomolecules, including carbohydrates, nucleic acids, lipids and proteins leading to an irreversibly destruction of the treated tissues. The diminution of TiO_2 NPs photoluminescence emissions would reduce its *in vivo* conditions capacity of ROS generation; leading to a better biocompatibility. Considering the biomedical applications that we want to impart to the prepared materials, the Ce-induced changes in their photoluminescence (PL) properties were evaluated. Pure anatase material (K1 sample) shows two PL-bands of different intensities centered at 287 nm and at 370 nm, ESI.[†] The weaker band at 287 nm can be attributed to a direct vertical transition of photo-induced electrons and holes in TiO_2 , while the stronger at 370 nm can be assigned to the band-to-band recombination because it is near-band-edge luminescence and/or to the exciton trapped at shallow-level defects.⁵⁶ In all CeO_2 – TiO_2 samples the PL-band placed at 287 nm disappeared whereas the intensity of the PL-band centered at 370 nm varied accordingly with the material $\text{Ce}(\text{Val})_3/\text{TTIP}$ proportion. A representation of % intensity of the PL-band peaked at 370 nm against the $\text{Ce}(\text{Val})_3/\text{TTIP}$ proportion, ESI,[†] shows a small increase of PL intensity followed by a drastic decrease at $\text{Ce}(\text{Val})_3/\text{TTIP}$ molar ratio $> 6 \times 10^{-3}$. Those facts are in total agreement with the previously discussed distortion of crystal anatase lattice due to Cerium atom incorporation.

3.2. Fibroblast–material interaction

Wound healing is an intricate process whereby a tissue or an organ repairs itself after injury.⁵⁷ Fibroblast participate in the fibroplasia and in the granulation tissue formation, the sequential and yet overlapping⁵⁸ phases of the wound healing classical model, by growing and forming a new provisional extracellular matrix (ECM) by excreting collagen and fibronectin.⁵⁹ They are also involved in fibrotic diseases, characterized by an excessive production, deposition and contraction of

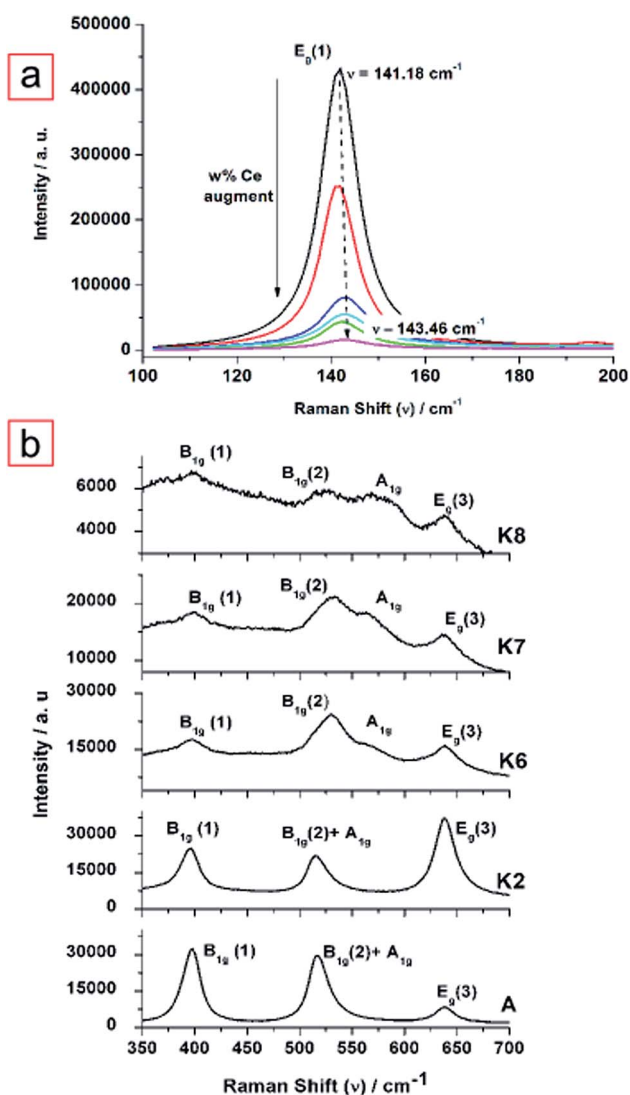


Fig. 8 Variation of anatase Raman vibration peaks intensity versus $\text{Ce}(\text{Val})_3/\text{TTIP}$ molar ratio: (a) $E_g(1)$ and (b) $B_{1g}(1)$, $B_{1g}(2)$ and A_{1g} Raman active modes.

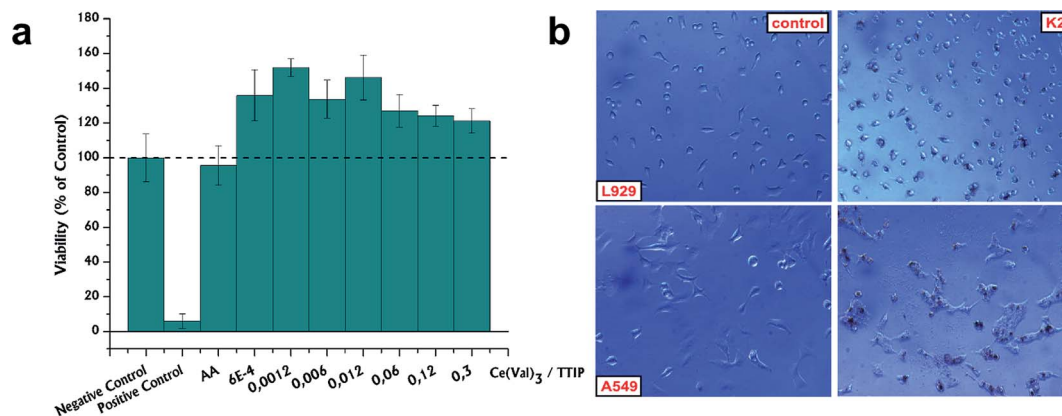


Fig. 9 (a) L929 fibroblasts viability after 24 hours of cell culture. (b) Morphology of L929 fibroblasts and A549 human lung epithelial cells, evaluated after 24 hours of cell culture in the presence of sample K4 (6.0×10^{-3} Ce(Val)₃/TTIP molar ratio).

extracellular matrix.^{60,61} For these reasons, and considering the possible applications of the prepared materials in the construction of calcified tissue implantable devices, it is very important to evaluate the interaction of the Ce-doped anatase fullerene-like structures with fibroblasts.

In a previous work¹⁵ we have investigated the effect of surface area, morphology and roughness on the Ce-doped anatase material–osteoblast interaction. The obtained results exclude any negative effect due to the crystalline microstructure, the morphology or the CeO₂ presence in osteoblast survival.¹⁵ Fig. 9a shows the cytotoxicity of the materials against L929 fibroblasts after 24 hours of cell culture by measuring the bio-reduction activity using PrestoBlue assay. In the presence of Ce-doped TiO₂ fullerene-like structures, fibroblast proliferation was significantly higher than the negative and positive controls, and than the proliferation in the presence of commercial TiO₂ anatase particles without a fullerene-like structure. In addition, fibroblast proliferation in contact with commercial anatase was 5% inferior to the negative control. A maximum in fibroblast proliferation can be achieved in the presence of the samples containing 1.2×10^{-3} –0.012 Ce/Ti molar ratio; lower and higher concentrations of cerium produced different cell proliferation, showing a Gaussian distribution. CeO₂ nanoparticles shows the ability to scavenge free radicals under physiological conditions⁴ that is comparable to those observed for superoxide dismutase⁶ and catalase.⁷ We have demonstrated that the oxygen storage capacity of the studied Ce-doped anatase materials accelerated the degradation of reactive nitroxide species (ONOO[−]) into less harmful types.¹⁵ Taking into account that reactive oxygen species balance is of particular importance in the proliferation of fibroblasts,⁶⁰ it is possible to argue that in specific Ce/Ti molar ratio conditions the material oxygen storage capacity would favour the fibroblast proliferation. Redox states have multiple significant but different cellular roles in the resistance and growth of lung tumors.⁶² Accordingly, we have decided to test the effect of the materials presence on adenocarcinomic human alveolar basal epithelial cells (A549) growth. This cellular line was regularly used to test particles viability.³² Epithelial cell proliferation in the presence

of the Ce-doped anatase materials decreased a 20% in comparison with negative control. Nevertheless proliferation was 60% superior than the positive control and than the proliferation in the presence of commercial TiO₂ anatase. Literature results report a 100% of viability of A549 cell in MoS₂ inorganic fullerene nanoparticles presence,³² demonstrating that in our case in addition of fullerene-like structure, there is a specific consequence of Ce–Ti presence on cellular propagation. During the process of adhesion and spreading in the presence of material, the cell morphology was similar to negative control for all tested samples; they showed their spindle-shaped forms with pseudopodial protrusions, such as filopodias, between them. Either in the presence of fibroblasts or epithelial cells, the material appears to be internalized by the cells after 24 h of contact, Fig. 9b. More results are shown in ESI.† Material–cell communication requires a system-specific interaction; the obtained result revealed a high viability and proliferation of osteoblast,¹⁵ fibroblast and A549 cell in the presence of the synthesised Ce-doped instead of commercial anatase. The precise contribution of fullerene-like Ce doped TiO₂ materials to fibroblast proliferation is still unclear; in part because of the difficulty of transferring information from primary studies into a growing appreciation of the complexity of the cellular environments. However, these studies have increased the general information of intricate interactions that would exist between an artificial device implanted in the human body and the host tissue. Given that fibrotic diseases might arise from a failure to suppress the normal wound healing response, the obtained results provide novel evidence and can address the definition of the appropriate conditions for their safe use of new inorganic scaffolds.

4. Conclusion

Here we demonstrated the effect of Ce-doped on the structure, photoluminescence emissions and oxygen storage capacity of TiO₂ anatase polymorphs. This concurrent effect indirectly favors the fibroblast proliferation. The incorporation of Ce(Val)₃ as ceria source during the synthesis of TiO₂ nanoparticles using

a microemulsion droplet system by way of a chemical micro-reactor, alters the crystalline planar distribution of TiO₂ lattice leading the attainment of crystals displaying a hollow, stable and closed structure; usually produced from compounds with (2D) layered arrangement. The presence of the cerium atoms is the folding driving force off the crystal planes and off the stabilization off anatase polymorph from the early steps of the synthesis. Large fullerene-type structures are obtained modulating the Ce/Ti molar ratio. Any negative effect of the material crystalline microstructure, morphology and CeO₂ presence on cell viability, morphology and adhesion was obtained. All tested material increased the fibroblast proliferation compared with control and with commercial anatase, this fact could be associated to its oxygen storage capacity.

Acknowledgements

The authors acknowledge Universidad Nacional del Sur (24/Q064), Concejo Nacional de Investigaciones Científicas y Técnicas de la República Argentina (CONICET, PIP-11220100100072.), ANG and JS have doctoral fellowships of CONICET. PVM is an independent researcher of CONICET. JMR thanks MICINN-Spain (Project MAT2011-25501). ANG thanks the Emerging Leaders in the Americas Program (ELAP).

References

- B. Choudhury and A. Choudhury, *Mater. Chem. Phys.*, 2012, **131**, 666–671.
- H. Gu and M. D. Soucek, *Chem. Mater.*, 2007, **19**, 1103–1110.
- A. S. Karakoti, N. A. Monteiro-Riviere, R. Aggarwal, J. P. Davis, R. J. Narayan, W. T. Self, J. McGinnis and S. Seal, *JOM*, 2008, **60**, 33–37.
- J. Dowding, S. Seal and W. Self, *Drug Delivery Transl. Res.*, 2013, 1–5.
- A. S. Karakoti, N. A. Monteiro-Riviere, R. Aggarwal, J. P. Davis, R. J. Narayan, W. T. Self, J. McGinnis and S. Seal, *JOM*, 2008, **60**, 33–37.
- I. Batinić-Haberle, in *Methods in Enzymology*, ed. P. Lester, Academic Press, 2002, vol. 349, pp. 223–233.
- B. J. Day, I. Fridovich and J. D. Crapo, *Arch. Biochem. Biophys.*, 1997, **347**, 256–262.
- E. G. Heckert, A. S. Karakoti, S. Seal and W. T. Self, *Biomaterials*, 2008, **29**, 2705–2709.
- M. Das, S. Patil, N. Bhargava, J.-F. Kang, L. M. Riedel, S. Seal and J. J. Hickman, *Biomaterials*, 2007, **28**, 1918–1925.
- F. Wauquier, L. Leotoing, V. Coxam, J. Guicheux and Y. Wittrant, *Trends Mol. Med.*, 2009, **15**, 468–477.
- Y. Hamada, H. Fujii and M. Fukagawa, *Bone*, 2009, **45**(suppl. 1), S35–S38.
- R. A. Gittens, T. McLachlan, R. Olivares-Navarrete, Y. Cai, S. Berner, R. Tannenbaum, Z. Schwartz, K. H. Sandhage and B. D. Boyan, *Biomaterials*, 2011, **32**, 3395–3403.
- M. Geetha, A. K. Singh, R. Asokamani and A. K. Gogia, *Prog. Mater. Sci.*, 2009, **54**, 397–425.
- D. Wei, Y. Zhou, D. Jia and Y. Wang, *Acta Biomater.*, 2007, **3**, 817–827.
- A. N. Gravina, J. M. Ruso, J. A. Laiuppa, G. E. Santillan, J. L. Marco-Brown, N. L. D'Elia and P. V. Messina, *J. Phys. Chem. B*, 2014, **2**, 834–845.
- M. Remskar, A. Mrzel, Z. Skraba, A. Jesih, M. Ceh, J. Demšar, P. Stadelmann, F. Lévy and D. Mihailovic, *Science*, 2001, **292**, 479–481.
- G. R. Samorodnitsky-Naveh, M. Redlich, L. Rapoport, Y. Feldman and R. Tenne, *Nanomedicine*, 2009, **4**, 943–950.
- M. N. Tahir, A. Yella, J. K. Sahoo, H. Annal-Therese, N. Zink and W. Tremel, *Phys. Status Solidi B*, 2010, **247**, 2338–2363.
- R. Tenne, *Chem.-Eur. J.*, 2002, **8**, 5296–5304.
- R. Tenne, L. Margulis, M. Genut and G. Hodes, *Nature*, 1992, **360**, 444–446.
- N. G. Chopra, R. J. Luyken, K. Cherrey, V. H. Crespi, M. L. Cohen, S. G. Louie and A. Zettl, *Science*, 1995, **269**, 966–967.
- Y. R. Hachon, E. Grunbaum, R. Tenne, J. Sloan and J. L. Hutchison, *Nature*, 1998, **395**, 336–337.
- A. N. Enyashin and G. Seifert, *Phys. Chem. Chem. Phys.*, 2007, **9**, 5772–5775.
- T. Kasuga, M. Hiramatsu, A. Hoson, T. Sekino and K. Niihara, *Langmuir*, 1998, **14**, 3160–3163.
- Á. Kukovecz, M. Hodos, E. Horváth, G. Radnóczy, Z. Kónya and I. Kiricsi, *J. Phys. Chem. B*, 2005, **109**, 17781–17783.
- J.-C. Chang, W.-J. Tsai, T.-C. Chiu, C.-W. Liu, J.-H. Chao and C.-H. Lin, *J. Mater. Chem.*, 2011, **21**, 4605–4614.
- S. Nosheen, F. S. Galasso and S. L. Suib, *Langmuir*, 2009, **25**, 7623–7630.
- T. Gao, H. Fjellvåg and P. Norby, *Inorg. Chem.*, 2009, **48**, 1423–1432.
- Y. G. Andreev and P. G. Bruce, *J. Am. Chem. Soc.*, 2008, **130**, 9931–9934.
- D. Wang, F. Zhou, Y. Liu and W. Liu, *Mater. Lett.*, 2008, **62**, 1819–1822.
- L. P. An, X. P. Gao, G. R. Li, T. Y. Yan, H. Y. Zhu and P. W. Shen, *Electrochim. Acta*, 2008, **53**, 4573–4579.
- H. Wu, R. Yang, B. Song, Q. Han, J. Li, Y. Zhang, Y. Fang, R. Tenne and C. Wang, *ACS Nano*, 2011, **5**, 1276–1281.
- M. Redlich, A. Gorodnev, Y. Feldman, I. Kaplan-Ashiri, R. Tenne, N. Fleischer, M. Genut and N. Feuerstein, *J. Mater. Res.*, 2008, **23**, 2909–2915.
- M. Redlich, A. Katz, L. Rapoport, H. D. Wagner, Y. Feldman and R. Tenne, *Dent. Mater.*, 2008, **24**, 1640–1646.
- A. Katz, M. Redlich, L. Rapoport, H. D. Wagner and R. Tenne, *Tribol. Lett.*, 2006, **21**, 135–139.
- N. Hassan, V. Verdinelli, J. M. Ruso and P. V. Messina, *Langmuir*, 2011, **27**, 8905–8912.
- P. V. Messina, V. Verdinelli, O. Pieroni and J. M. Ruso, *Colloid Polym. Sci.*, 2013, **291**, 835–844 and references therein.
- J. M. Ruso, A. N. Gravina, N. L. D'Elia and P. V. Messina, *Dalton Trans.*, 2013, 7991–8000.
- A. Bumajdad, J. Eastoe and A. Mathew, *Adv. Colloid Interface Sci.*, 2009, **147–148**, 56–66.
- C. Yang, F. Chen, S. Luo, G. Xie, G. Zeng and C. Fan, *J. Hazard. Mater.*, 2010, **175**, 187–192.

- 41 G. Palazzo, F. Lopez, M. Giustini, G. Colafemmina and A. Ceglie, *J. Phys. Chem. B*, 2003, **107**, 1924–1931.
- 42 R. A. Spurr and H. Myers, *Anal. Chem.*, 1957, **29**, 760–762.
- 43 *Crystals and Crystal Structures*, ed. R. J. D. Tilley, John Wiley & Sons Ltd, The Atrium, Southern Gate, Chichester, West Sussex PO19 8SQ, England, 2006.
- 44 M. Calatayud, P. Mori-Sánchez, A. Beltrán, A. Martín Pendás, E. Francisco, J. Andrés and J. M. Recio, *Phys. Rev. B: Condens. Matter Mater. Phys.*, 2001, **64**, 184113.
- 45 A. Fahmi, C. Minot, B. Silvi and M. Causá, *Phys. Rev. B: Condens. Matter Mater. Phys.*, 1993, **47**, 11717–11724.
- 46 T. López, F. Rojas, R. Alexander-Katz, F. Galindo, A. Balankin and A. Buljan, *J. Solid State Chem.*, 2004, **177**, 1873–1885.
- 47 R. Shannon, *Acta Crystallogr., Sect. A: Cryst. Phys., Diffraction, Theor. Gen. Crystallogr.*, 1976, **32**, 751–767.
- 48 C. Fu, T. Li, J. Qi, J. Pan, S. Chen and C. Cheng, *Chem. Phys. Lett.*, 2010, **494**, 117–122.
- 49 B. J. Morgan and G. W. Watson, *J. Phys. Chem. C*, 2010, **114**, 2321–2328.
- 50 J. Fang, H. Bao, B. He, F. Wang, D. Si, Z. Jiang, Z. Pan, S. Wei and W. Huang, *J. Phys. Chem. C*, 2007, **111**, 19078–19085.
- 51 C.-H. Yang and Z.-Q. Ma, *Appl. Opt.*, 2012, **51**, 5438–5441.
- 52 O. Frank, M. Zúkalova, B. Laskova, J. Kurti, J. Koltai and L. Kavan, *Phys. Chem. Chem. Phys.*, 2012, **14**, 14567–14572.
- 53 P. Periyat, K. V. Baiju, P. Mukundan, P. K. Pillai and K. G. K. Warriar, *J. Sol-Gel Sci. Technol.*, 2007, **43**, 299–304.
- 54 M. S. P. Francisco and V. R. Mastelaro, *Chem. Mater.*, 2002, **14**, 2514–2518.
- 55 Y. Li, W. Zhang, J. Niu and Y. Chen, *ACS Nano*, 2012, **6**, 5164–5173.
- 56 J. M. Ruso, V. Verdinelli, N. Hassan, O. Pieroni and P. V. Messina, *Langmuir*, 2013, **29**, 2350–2358.
- 57 D. T. Nguyen, D. P. Orgill and G. F. Murphy, in *Biomaterials For Treating Skin Loss*, Woodhead Publishing (UK/Europe) & CRC Press (US), Cambridge/Boca Raton, 2009, ch. 4, pp. 25–57.
- 58 W. K. Stadelmann, A. G. Digenis and G. R. Tobin, *Am. J. Surg.*, 1998, **176**, 26S–38S.
- 59 K. S. Midwood, L. V. Williams and J. E. Schwarzbauer, *Int. J. Biochem. Cell Biol.*, 2004, **36**, 1031–1037.
- 60 G. A. Murrell, M. J. O. Francis and L. Bromley, *Biochem. J.*, 1990, **265**, 659–665.
- 61 A. Leask and D. J. Abraham, *FASEB J.*, 2004, **18**, 816–827.
- 62 J. C.-M. Ho, S. Zheng, S. A. A. Comhair, C. Farver and S. C. Erzurum, *Cancer Res.*, 2001, **61**, 8578–8585.